Journal of Thermal Analysis and Calorimetry (2024) 149:7973–7985
https://doi.org/10.1007/s10973-024-13267-5

Assessment of Ce-rich intermetallics formation in Al-Cu-Mg-xCe alloys using thermal analysis cooling curves

H. Mohammadi[1] · R. Taghiabadi[2] · M. Malekan[3]

Received: 11 December 2023 / Accepted: 1 May 2024 / Published online: 18 May 2024

Abstract
The computer-aided cooling curve analysis (CA-CCA) was employed to investigate the solidification behavior of Al-Ce-Mg-xCe ($x = 0$, 0.5, 1.0, 1.5, and 3.0 mass %) alloys. Field emission scanning electron microscopy (FE-SEM), energy-dispersive X-ray spectroscopy (EDS), and X-ray diffraction (XRD) techniques were used, along with the liquidus projection of ternary Al-Cu-Mg and Al-Cu-Ce phase diagrams, to evaluate the microstructure and predict the sequence of main reactions involved in the solidification of alloys. According to the results, Al_2CuMg, Al_2Cu, $Al_{15}(CuFeMn)_3Si_2$, and Mg_2Si were found to be the main compounds present in the microstructure of Al 2024 alloy. The addition of Ce up to 1.5 mass % resulted in the formation of AlCeCuSi, Al_8CeCu_4, and $Al_{24}Cu_8Ce_3Mn$ compounds in the microstructure. Further addition of Ce up to 3.0 mass % promoted the formation of a new Ce-rich phase (Al_4Ce) in the microstructure. The formation temperature (range) and reactions during which the Ce-rich compounds are formed were also suggested. The formation of Al_4Ce compound in the microstructure of 3 mass % Ce-containing samples suppressed the nucleation and growth temperatures of the Al_2Cu eutectic, prolonged the solidification time, significantly reduced the solidification end temperature, and increased the alloy solidification range.

Keywords Thermal analysis · Cooling curve · First derivative curve · Al 2024 · Microstructure · Cerium

Introduction

Owing to the low density, high tensile strength, good ductility, high damage tolerance, and good fracture toughness, the Al 2024 alloy is a promising candidate for applications requiring high specific strength such as aerospace and transportation [1, 2]. However, due to the presence of various alloying elements such as Cu, Mg, and Mn and impurities such as Fe and Si in its composition, this alloy exhibits a complex microstructure comprising different intermetallic compounds such as Al_2Cu, Al_2CuMg, Mg_2Si, Al_7Cu_2Fe, and $Al_{20}Cu_2Fe$ [3]. These intermetallics are reported to exert undeniable effects on the castability, physical, mechanical, and corrosion properties of Al 2024 alloy [1, 3]. Therefore, it is vitally important to understand their type, geometrical characteristics, and distribution across the alloy microstructure.

Among the rare earth elements, Ce due to its lower price and proven effectiveness has been considered for the microstructural modification and properties enhancement of several engineering alloys [4]. It was found that the addition of Ce improves the alloy's performance by forming high-melting point and stable Ce-rich intermetallics, microstructural refinement [5, 6], and modification of existing intermetallics/second phases through changing their solidification sequence, poisoning, etc. [6–8]. Xiao et al. improved the tensile strength of Al-5.3Cu-0.8Mg-0.6Ag [9] and Al5.3Cu-0.8Mg-0.6Ag-0.4Mn-0.1Zr [10] by the addition of 0.2 and 0.45 mass % Ce, respectively. They attributed these to the formation of finer and denser θ-Al_2Cu and θ′-Al_2Cu compounds within the alloys microstructure. Yu et al. [11] demonstrated the beneficial effect of Ce (0.25 mass %) on the fracture toughness of Al-4.6Cu-0.4Ag-1.3Li-0.4Mg-0.13Zr alloy. This improvement was explained by the formation of fine Al_8Cu_4Ce

✉ R. Taghiabadi
taghiabadi@ikiu.ac.ir

[1] Department of Metallurgy and Materials Science, Imam Khomeini International University, Qazvin, Iran

[2] Department of Metallurgy and Materials Science, Imam Khomeini International University, Qazvin, Iran

[3] School of Metallurgy and Materials Engineering, University of Tehran, Tehran, Iran

precipitates along the alloy grain boundaries. Wang and his colleagues [12] found that the addition of 0.2 mass % Ce due to encouraging the formation of denser and finer θ′-Al_2Cu compounds enhanced both room and high temperature tensile strength of AA2519 Al alloy. They also reported that the addition of 0.4 mass % Ce due to the formation of high-melting point Al_8Cu_4Ce phase increased elevated temperature mechanical properties of the alloy. Recently, Vončina et al. [13] tried to modify the as-cast and brittle microstructure of Al-1.4 mass % Fe by the addition of 0.15 mass % Ce. According to their results, Ce addition refined the α-Al grains but could not modify the morphology of the eutectic Al_xFe_y. Ce-containing eutectics were also reported to improve casting properties and thermal stability of wrought Al alloys [14, 15]. According to Guodong et al. [16], the addition of 0.3 mass % Ce refined α-Al grains, modified the eutectic Si particles and improved the alloy fluidity by about 40%.

A brief literature survey indicates that efforts have been made so far on the effect of Ce on the microstructure [17–20], mechanical properties [17, 18], and corrosion behavior [19] of various engineering alloys. However, to the best of authors' knowledge, no systematic study has been undertaken so far on solidification characteristics and microstructure evolution of Ce-added Al 2024 alloys. Considering its negligible solid-solubility in α-Al [21], the addition of Ce is likely to have significant effects on the solidification behavior and microstructure of the Al 2024 alloy by changing the type and composition of existing intermetallics and encouraging the formation of new Ce-rich compounds within the alloy microstructure.

The computer-aided cooling curve analysis (CA-CCA) is a low-cost, fast, and verified method, capable of online analysis of alloys solidification at cast-shops [22–24]. Moreover, the CA-CCA gives us this opportunity to obtain consistent and comprehensive information regarding the thermo-physical behavior of alloys such as solidification time, fraction of solid, solidification temperature range, dendrites coherency point, latent heat, and nucleation and growth temperature of individual phases (intermetallics) [25, 26]. These features make CA-CCA preferable to other thermal analysis methods such as differential thermal analysis (DTA) in obtaining solidification characteristics of alloys in relation to their microstructure.

In spite of extensive research on the cooling curve thermal analysis of various cast and wrought Al alloys, a review of the literature reveals limited works concerning the application of CA-CCA in investigating the microstructure and solidification behavior of Al 2024 alloy. Shabestari et al. [3] tried to evaluate the formation of intermetallic compounds such as Al_2Cu, $Al_{15}(CuFeMn)_3Si_2$, $Al_{20}Cu_2Mn_3$, Mg_2Si, and Al_2CuMg in the microstructure of Al 2024 alloy with the help of CA-CCA. Ghoncheh et al. [27] investigated the effect of cooling rate on the microstructure and solidification behavior of Al 2024 alloy by using CA-CCA. In other works [26, 28], the effects of cooling rate and grain refinement on the hot tearing sensitivity of Al 2024 alloy were studied. In these studies, the dendrite coherency point and critical solidification temperatures were determined by CA-CCA. Amin et al. [29] also used CA-CCA to evaluate the microstructure of a squeezed cast Al-4Cu alloy.

Considering the potentially broad impact of the type, geometrical parameters, and the distribution of Ce-rich intermetallic compounds on the properties of Ce-added Al-Cu-Mg alloys such as room and high mechanical properties, corrosion resistance, and hot tearing susceptibility, investigating the temperature and sequence of reactions during which these compounds are formed is highly important. On this basis, CA-CCA was used for the first time to thermally analyze the solidification behavior, predict the main reaction sequences involved, and investigate phase evolution in Ce-added Al 2024 alloy. It was also attempted to verify the CA-CCA results by the FE-SEM, EDS, and XRD investigations.

Material and methods

The chemical composition of the as-received Al 2024 alloy is illustrated in Table 1. To prepare experimental alloys containing different amounts of Ce (0.5, 1.0, 1.5, and 3.0 mass %), 250 g of Al 2024 ingot was melted in a clay-graphite crucible using an electric resistance furnace at 750 ± 5 °C. After melting the alloy, the required amount of Ce was added to the melt by using an Al-30Ce master alloy. The chemical composition of Ce-added alloys determined by the XRF method are also illustrated in Table 1. Before conducting thermal analysis tests, the melts were kept for 5 min and then gently stirred by a graphite rod for about 2 min to be

Table 1 Chemical composition (in mass %) of the experimental alloys

Alloy code	Cu	Mg	Mn	Fe	Si	Ce	Al
2024	4.38	1.54	0.44	0.14	0.13	–	Bal
0.5Ce	4.31	1.51	0.42	0.13	0.12	0.52	Bal
1Ce	4.23	1.48	0.42	0.13	0.12	1.13	Bal
1.5Ce	4.17	1.46	0.41	0.13	0.11	1.49	Bal
3Ce	4.01	1.39	0.39	0.14	0.11	3.07	Bal

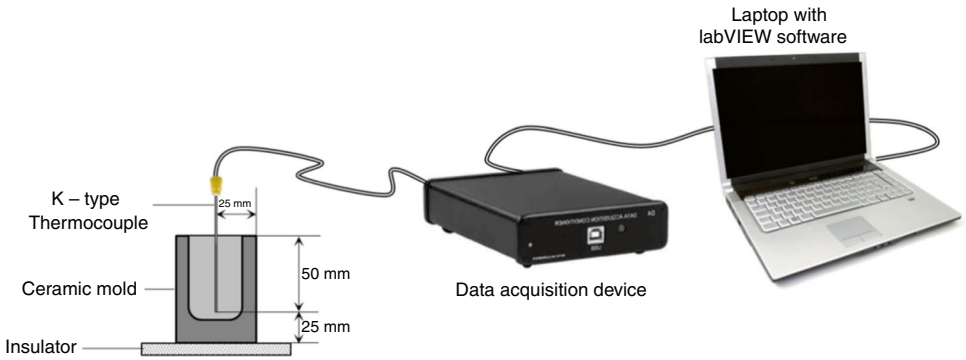

Fig. 1 Schematic diagram showing the setup of CA-CCA

homogenized. After skimming the surface dross, the melt was poured into a mold while an insulated high-sensitivity K-type thermocouple was placed in its center (Fig. 1). The rapid cooling rate makes it difficult to detect slight temperature changes. Therefore, to avoid missing minor peaks, all experiments were conducted in a ceramic mold with an average cooling rate of about $0.4°Cs^{-1}$. The samples were coded as XCe where X denotes the average Ce concentration in mass %.

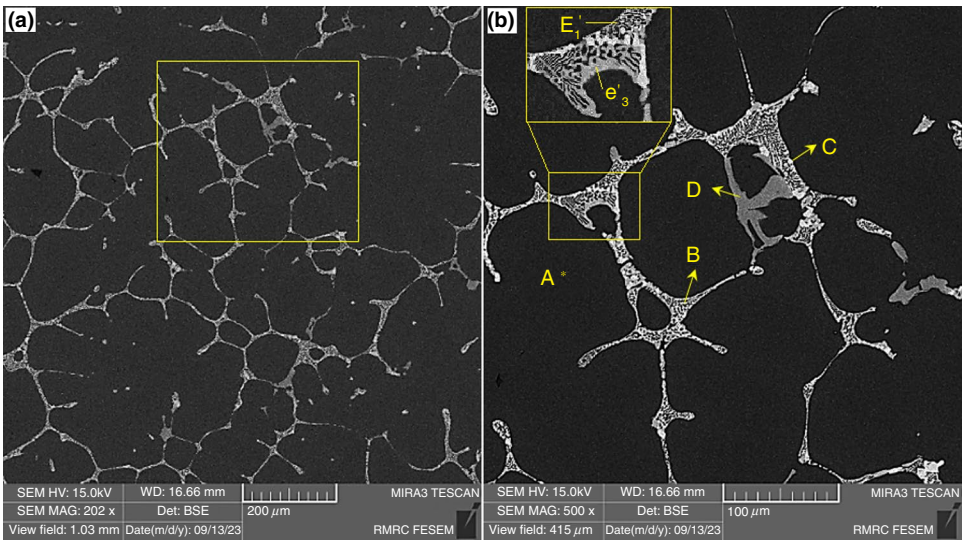

Fig. 2 **a** SEM micrograph showing the as-cast microstructure of Al 2024 alloy and **b** enlarged view of the boxed zone in Fig. 2a

Table 2 EDS analysis of observed phases in the microstructure of Al 2024 alloy in Fig. 2b

Point	Elements/mass %							Predicted phases	Reference
	Cu	Ce	Mn	Mg	Fe	Si	Al		
A	1.24	–	–	3.02	–	0.85	94.89	α–Al	Current work
B	28.60	–	–	6.71		–	64.68	Al_2CuMg	Current work
	17.33	–	–	10.73	–	–	71.54		[26]
	42.0	–	–	11.8	–	–	46.2		[33]
C	48.97	–	–	–	–	–	51.03	Al_2Cu	Current work
	29.86	–	–	–	–	–	70.14		[26]
	51.5	–	–	–	–	–	48.5		[33]
D	5.90	–	9.29	–	15.48	5.12	64.22	$Al_{15}(CuFeMn)_3Si_2$	Current work
	3.78	–	4.17	–	10.20	11.98	69.87		[26]
	3.73	–	4.14	–	10.21	11.94	69.93		[3]

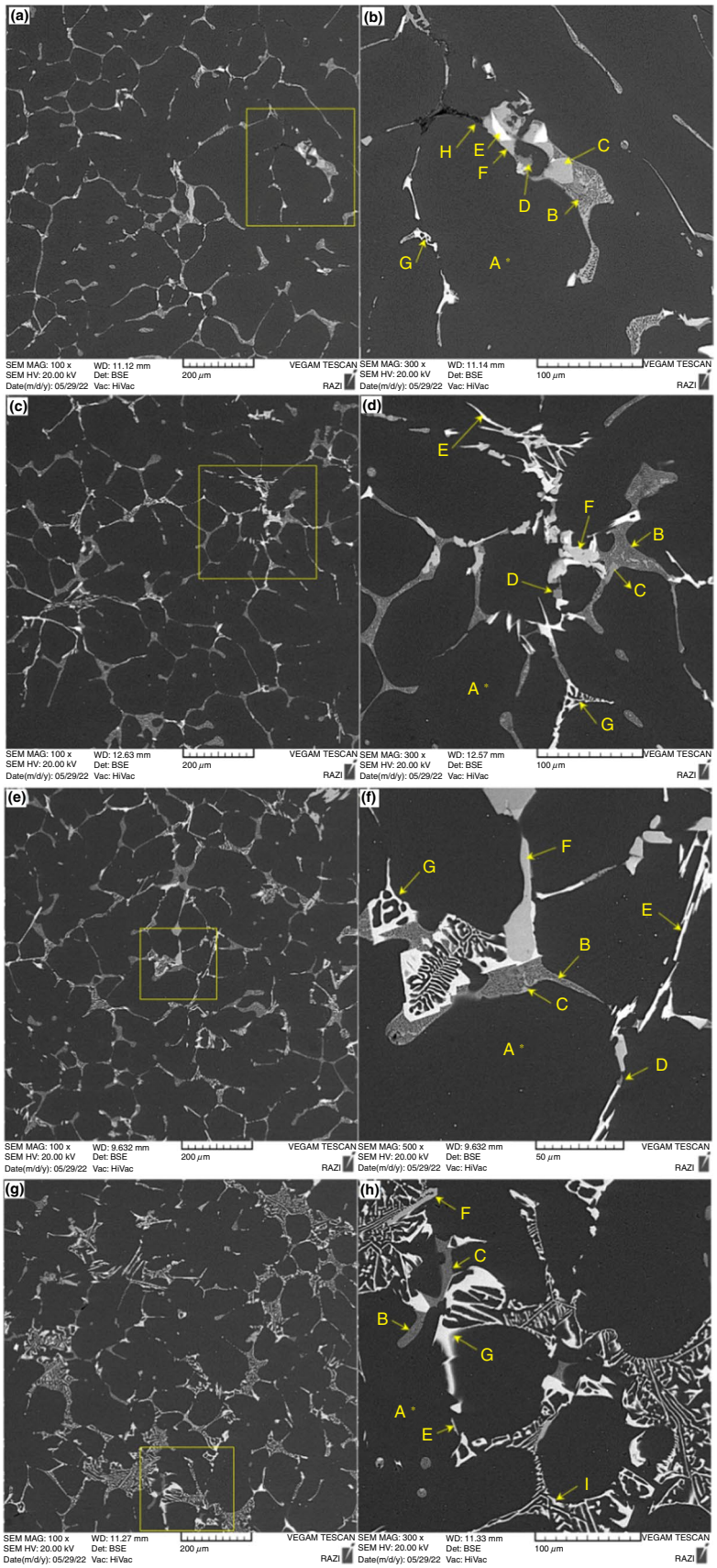

Fig. 3 SEM micrographs showing the effect of Ce content on the microstructure of Al 2024 alloy, **a**,**b** 0.5 mass % Ce, **c**,**d** 1.0 mass %, **e**,**f** 1.5 mass % Ce, **g**,**h** 3.0 mass % Ce

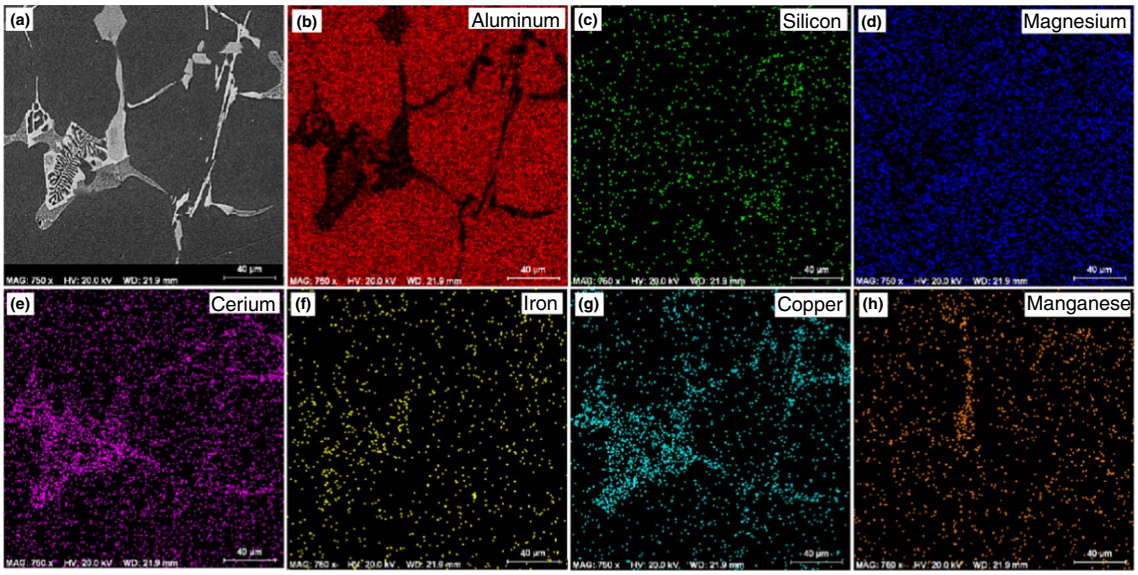

Fig. 4 Backscattered SEM micrograph and series of elemental maps showing the distribution of key elements in intermetallic compounds of the 1.5Ce sample

Before tests, the thermocouple was calibrated by analyzing the solidification of a high-purity (99.9 mass %) molten Al. An analog-to-digital converter with a sensitive 16-bit converter, a resolution of 0.0015%, and a response time of 0.02 s was used to convert the analog signals into digital signals. The thermocouple was connected to a high-speed data collection device capable of recording five data per second (Fig. 1). The temperature measurement error of the employed thermocouple was also about ± 1 °C. The processing of the thermal analysis data including plotting cooling curves, first derivative curves, smoothing and fitting of curves, identifying the onset and end of the solidification process, and determining solidification parameters such as the cooling rate, the nucleation temperature, the solidification range, and the total solidification time was performed by Origin Pro 2022 software.

Metallography samples were prepared from the thermally analyzed samples at the nearest location to the thermocouple tip. The surface preparation of samples was performed by grinding with SiC abrasive paper from P120 to P2500 grade followed by diamond paste polishing up to 1 µm to produce a mirror-like surface followed by chemical etching by a Keller's reagent (2.5 mL HNO_3 + 1.5 mL HCl + 1 mL HF + 95 mL distilled water) for 10 s to reveal the microstructure. A MIRA3-TESCAN FE-SEM equipped with an EDS system was used to identify/analyze microstructural phases. The image analysis of microstructures was performed using Digimizer 5.3.5 software. An X-ray diffractometer (XRD) (GNR APD 2000) was also employed to identify phases present in the microstructure. XRD patterns were obtained by using a continuous scan mode and 2θ angle of 25 to 80 degrees with a sampling width of 0.02 degrees and a scanning speed of 1 degmin^{-1}. In order to better reveal weak peaks, before the XRD analysis all samples were deep etched using 30 vol. % H_2SO_4 + 70 vol. % distilled water solution followed by ultrasonic cleaning with acetone in an ultrasonic bath.

Results and discussion

Microstructure evaluation and phase analysis

Figure 2 depicts the as-cast microstructure of the Al 2024 alloy at two different magnifications. It is evident that the alloy microstructure consists of different phases whose EDS analyses are presented in Table 2. According to the EDS analysis and in agreement with previous reports presented in Table 2, the main phases present in the microstructure of unmodified Al 2024 alloy are θ-Al_2Cu (tetragonal, a = 6.06 Å, c = 4.87 Å) [30] and S-Al_2CuMg (orthorhombic, a = 4.01 Å, b = 9.23 Å, and c = 7.14 Å) [31] which are distributed within an α-Al matrix. It is worth noting that, due to the presence of small amounts of Si and Fe impurities in the alloy composition (Table 1), the Mg_2Si (FCC antifluorite, a = 6.338 Å) [32] and α-Fe(Mn) compounds are also likely to be observed in the microstructure.

The effect of Ce addition (0.5, 1.0, 1.5, and 3.0 mass %) on the microstructure of Al 2024 alloy is shown in Fig. 3. As it can be seen, due to the near-zero solid-solubility of Ce in Al (maximum 0.00005 mass % [34]) its addition resulted in

Table 3 EDS analysis of the phases observed in the microstructure of Ce-added Al 2024 alloys in Fig. 3

Ce content/mass %	Point	Elements/mass %							Predicted phases
		Cu	Ce	Mn	Mg	Fe	Si	Al	
0.5 (Fig. 3a,3b)	A	2.38	1.03	1.53	1.88	–	–	93.18	α-Al
	B	27.15	–	–	10.14		–	62.71	Al_2CuMg
	C	53.51	–	–	0.71		–	45.78	Al_2Cu
	D	10.48	–	14.33	–	15.63	2.52	57.04	$Al_{15}(CuFeMn)_3Si_2$
	E	31.32	33.86	–	0.54		6.09	28.19	AlCeCuSi
	F	28.32	18.92	6.23	0.56	–	–	45.97	$Al_{24}Cu_8Ce_3Mn$
	G	41.32	18.78	–	–	–	–	39.90	Al_8CeCu_4
	H	–	–	–	57.32	–	35.67	7.01	Mg_2Si
1 (Fig. 3c,3d)	A	2.34	1.44	0.25	1.45	–	0.83	93.69	α-Al
	B	32.83	–	–	8.78		–	58.39	Al_2CuMg
	C	53.51	–	–	0.71		–	45.78	Al_2Cu
	D	11.23	0.63	12.78	–	14.43	3.45	57.48	$Al_{15}(CuFeMn)_3Si_2$
	E	27.03	35.61	–	–		5.64	31.72	AlCeCuSi
	F	27.20	20.21	5.52	1.66		–	45.41	$Al_{24}Cu_8Ce_3Mn$
	G	42.09	16.88	–	–		–	41.03	Al_8CeCu_4
1.5 (Fig. 3e,3f)	A	2.03	1.55	0.33	1.95	0.28	0.71	93.18	α-Al
	B	32.83	–	–	8.78	–	–	58.39	Al_2CuMg
	C	53.51	–	–	0.71	–	–	45.78	Al_2Cu
	D	12.68	1.02	13.26	–	16.79	4.58	51.67	$Al_{15}(CuFeMn)_3Si_2$
	E	27.03	35.61	–	–	–	5.64	31.72	AlCeCuSi
	F	27.20	20.21	5.52	1.66	–	–	45.41	$Al_{24}Cu_8Ce_3Mn$
	G	42.09	16.88	–	–		–	41.03	Al_8CeCu_4
3 (Fig. 3g,3h)	A	2.94	2.45	0.76	1.65	0.32	0.29	91.59	α-Al
	B	32.83	–	–	8.78	–	–	58.39	Al_2CuMg
	C	53.51	–	–	0.71	–	–	45.78	Al_2Cu
	E	28.03	32.61	–	–	–	4.25	35.11	AlCeCuSi
	F	29.54	19.93	6.24	0.83	–	–	43.46	$Al_{24}Cu_8Ce_3Mn$
	G	42.09	16.88	–	–	–	–	41.03	Al_8CeCu_4
	I	2.45	45.26	–	–	–	–	52.29	Al_4Ce

Table 4 EDS composition of the main Ce-rich compounds detected in the microstructure of Al 2024 alloys presented in other studies

Phase	Elements/mass %						References
	Cu	Ce	Mn	Mg	Si	Al	
Al_8CeCu_4	41.66	22.96	–	–	–	35.38	[35]
	43.5	22.2	–	–	–	34.3	[36]
	42.5	19.2	–	–	–	38.3	[4]
Al_4Ce	–	58.62	–	–	–	41.38	[35]
	3.8	54.5	–	–	–	41.7	[36]
	–	56.5	–	–	–	43.5	[37]

the formation of various randomly distributed bright phases in the microstructure whose fraction is increased by the Ce content. The EDS mapping result showing the elemental distribution of Al, Cu, Mg, Ce, Mn, Si, and Fe within the microstructure of 1.5Ce alloy is shown in Fig. 4. The chemical composition of main microstructural phases determined by the EDS method is shown in Table 3. For comparison, the EDS analyses of two main Ce-containing compounds obtained by other researchers are also presented in Table 4.

According to EDS analysis (Table 3), it seems that the predominant phases present in the microstructure of 0.5, 1.0, and 1.5 mass % Ce-containing samples are Al_2Cu, AlCeCuSi ($Al_9Ce_2Cu_5Si_3$), and Al_8CeCu_4 (tetragonal, $a = 8.85$ Å, $c = 5.18$ Å [37]) along with other Cu- and Ce-rich intermetallics such as Al_2CuMg, and $Al_{24}Cu_8Ce_3Mn$, and small

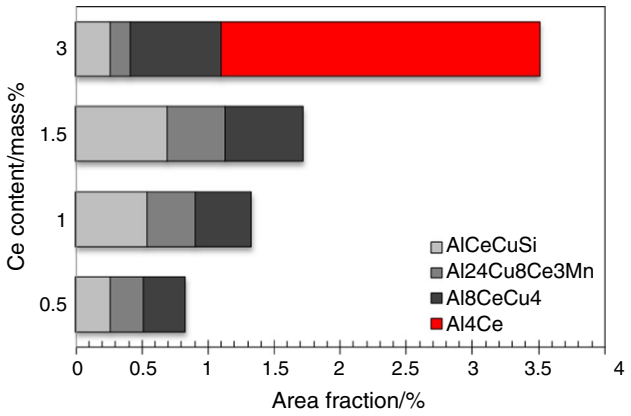

Fig. 5 Effect of Ce content on the fraction of Ce-rich compounds in the microstructure of Al 2024 alloy

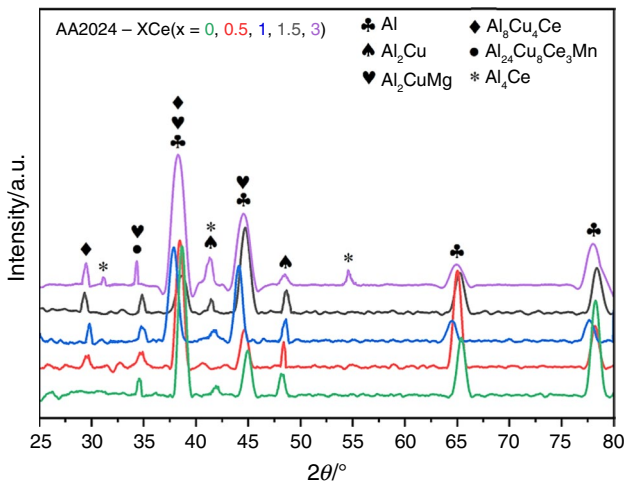

Fig. 6 X-ray diffraction patterns of Ce-added Al 2024 alloys

amounts of Mg_2Si which are distributed in an α-Al matrix. In addition, a new phase composed of Al and Ce (Al_4Ce) is also detected as an interconnected eutectic microstructure in 3.0 mass % Ce-containing sample which is concordant with the previous studies [38]. The effect of Ce content on the fraction of main Ce-rich compounds in the microstructure of Ce-added Al 2024 alloys is shown in Fig. 5. As it can be seen, increasing the Ce content up to about 1.5 mass % expectedly increased the fraction of AlCeCuSi ($Al_9Ce_2Cu_5Si_3$), $Al_{24}Cu_8Ce_3Mn$ and Al_8CeCu_4 compounds in the microstructure. Further addition of Ce up to about 3.0 mass % increased the fraction of Al_8CeCu_4 compound by about 20%. But probably due to the formation of new Ce-rich phase Al_4Ce and the significant consumption of Ce atoms, the fraction of AlCeCuSi and $Al_{24}Cu_8Ce_3Mn$ phases in 3.0Ce sample has decreased.

The results obtained by FE-SEM/EDS analysis were further confirmed by the XRD characterization. Figure 6 shows XRD patterns of 2024-xCe ($x = 0$, 0.5, 1.0, 1.5, and 3.0 mass %) alloys which demonstrate the presence of α-Al, Al_2Cu, Al_2CuMg, $Al_{24}Cu_8Ce_3Mn$, and Al_8CeCu_4 in samples with the Ce content of ≤ 1.5 mass %, and α-Al, Al_2Cu, Al_2CuMg, $Al_{24}Cu_8Ce3Mn$, Al_8CeCu_4, and Al_4Ce (orthorhombic, $a = 4.39$ Å, $b = 13.02$ Å, $c = 10.09$ Å [37]) phases in the alloy containing 3 mass % Ce.

Computer-aided cooling curve analysis

Solidification cooling curves and respective first derivative curves corresponding to the Al 2024-xCe ($x = 0.0$, 1.0, 1.5, and 3.0 mass %) alloys are shown in Fig. 7. It is worth noting that, due to the similarity of the cooling curves of the 0.5Ce and 1Ce samples, the cooling curve of the former is not presented in this figure. As is well known, upon the onset of the crystallization of each phase, the latent heat evolved decreases the solidification rate and affects the cooling curve by local decreasing its gradient. However, situations are encountered where thermal signals are so weak and it is practically hard to properly detect them on the cooling curve. In these situations, the first derivative curve is applied to provide conditions for a more accurate identification of characteristic features of the cooling curve. Indeed, the appearance of sudden peaks in a first derivative curve implies a phase transformation.

Considering the liquidus projection of the Al-rich corner of the Al-Cu-Mg phase diagram (Fig. 8) and the Scheil non-equilibrium solidification model [37], the solidification of the experimental Al 2024 alloy begins with the nucleation of primary α-Al dendrites at about 640 °C. Following the development of the dendritic network, the solidification process continues by the quasi-binary eutectic reaction e'_3 (24.5 mass % Cu and 10.1 mass % Mg [37]) and the ternary eutectic reaction of E'_1 (30 mass % Cu and 6 mass % Mg [36]).

The above predicted reactions are also detected by the CA-CCA. According to Fig. 7a, the solidification of Al 2024 alloy starts with the nucleation of α-Al dendrites (the dark gray dendritic matrix in Fig. 2) at a temperature of about 640 °C (T_N) which manifests itself as a sudden peak (the first peak) in the corresponding first derivative curve (Fig. 7a). The binary eutectic reaction e'_3 appears as another peak (peak #3) in the temperature range of 512–501 °C. The product of this reaction is seen as a Chinese-script eutectic composed of dark gray α-Al and rather light gray Al_2CuMg phases in the microstructure (Fig. 2b).

According to SEM micrographs 2a and 2b, EDS analysis results (Table 2), and in confirmation of the solidification sequence of the alloy (Fig. 8), the coexistence of S-Al_2CuMg (the rather light gray networks in Fig. 2b) with θ-Al_2Cu (the bright polygonal particles in Fig. 2b), and Mg_2Si (dark phase) suggests that they are probably crystallized

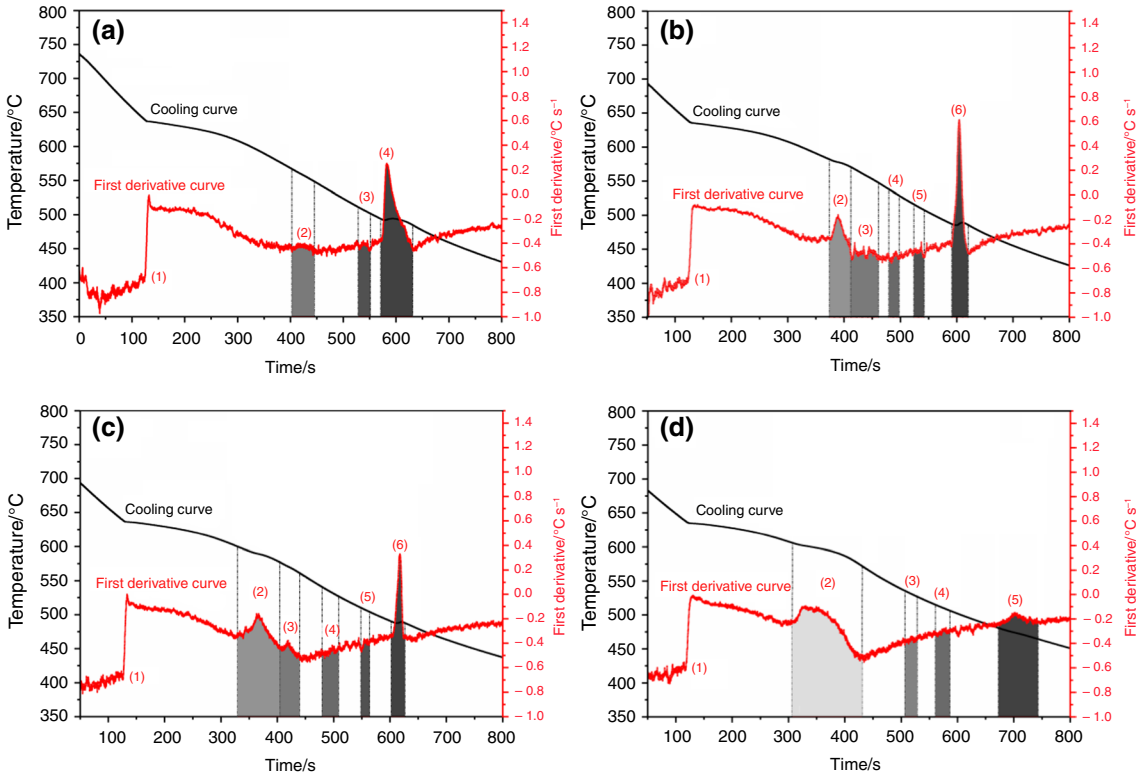

Fig. 7 Thermal analysis curves of Ce-added Al 2024 alloys **a** Al 2024, **b** 1Ce, **c** 1.5Ce, and **d** 3.0Ce samples

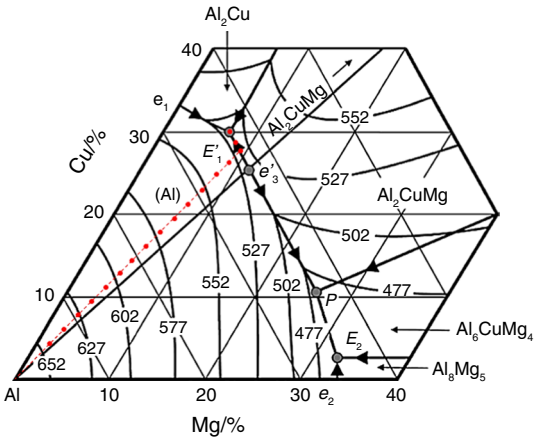

Fig. 8 Liquidus projection of Al-rich corner of Al-Cu-Mg ternary phase diagram [37]. The solidification path line corresponding to the base alloy obtained based on the Scheil non-equilibrium solidification approach is shown on the diagram

Table 5 Predicted solidification sequences during the solidification of the Al 2024 alloy at the cooling rate of 0.4°Cs^{-1}

Reaction no	Chemical reaction	Temperature range/°C
1	L → α-Al dendritic networks	640
2	L → α-Al + $Al_{15}(CuFeMn)_3Si_2$ + $Al_{20}Cu_2Mn_3$ L + $Al_{20}Cu_2Mn_3$ → α-Al + Al_2Cu + $Al_{15}(CuFeMn)_3Si_2$	570–545
3	e′3: L → α-Al + Al_2CuMg	512–501
4	E′1: L → α-Al + Al_2CuMg + Al_2Cu + Mg_2Si	493–483

concurrently through another eutectic reaction at last stages of the alloy solidification. The occurrence of this eutectic reaction (E'_1) in the temperature range of 493–483 °C was also predicted by CA-CCA in Fig. 7a which is associated with a sharp peak in the first derivative curve (peak #4).

In addition to the above-discussed peaks, there is also another noticeable peak (peak #2) in the first derivative curve of Al 2024 alloy. Considering the presence of Mn, Fe, and Si in the alloy composition and in agreement with the previous findings [3], this peak is probably related to another binary eutectic reaction L → α-Al + $Al_{15}(CuFeMn)_3Si_2$ + $Al_{20}Cu_2Mn_3$ which is expected to occur in the temperature range of 570–545 °C. Moreover, based on Mondolfo's assumption [39], the $Al_{20}Cu_2Mn_3$ compound is an unstable phase that converted to Al_2Cu and $Al_{15}(CuFeMn)_3Si_2$ through a hypothetical peritectic reaction (Table 5). The $Al_{15}(CuFeMn)_3Si_2$ compound is indicated in Fig. 2b. Relevant reactions of Al 2024 alloy are summarized in Table 5.

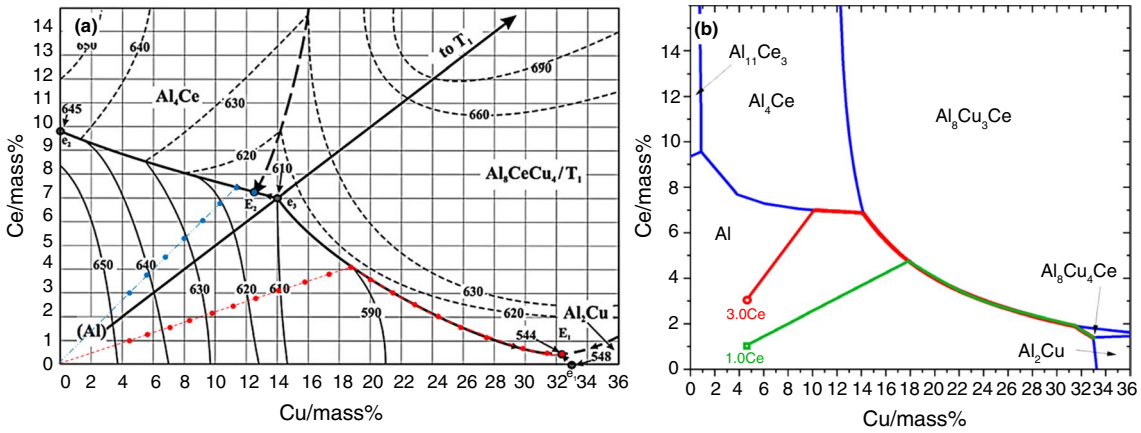

Fig. 9 Liquidus projection of Al-rich corner of the Al-Cu-Ce ternary phase diagram [36], **b** the calculated diagram proposed by Perrin et al. [35]. The solidification path lines corresponding to the 1Ce and 3.0Ce alloys obtained based on the Scheil non-equilibrium solidification approach are shown in the diagrams

Table 6 Predicted solidification sequences in 1Ce and 1.5Ce samples at the cooling rate of 0.4°Cs^{-1}

Reaction(s) No	Chemical reactions	Reaction temperature (range)/°C	
		1Ce	1.5Ce
1	L → α-Al dendritic networks	640	640
2	L → α-Al + Al_8CeCu_4 (Al_8CeCu_3[a])	582–569	603–577
3	L → α-Al + $Al_{15}(CuFeMn)_3Si_2$ + $Al_{20}Cu_2Mn_3$ L + $Al_{20}Cu_2Mn_3$ → α-Al + Al_2Cu + $Al_{15}(CuFeMn)_3Si_2$	569–547	577–557
4	L → α-Al + Al_8CeCu_4 + Al_2Cu	538–528	538–529
5	e′3: L → α-Al + Al_2CuMg	514–507	510–503
6	E′1: L → α-Al + Al_2CuMg + Al_2Cu + Mg_2Si	486–485	489–486

[a]Based on the modified liquidus projection of the Al-rich corner of the Al-Cu-Ce ternary phase diagram (Fig. 9b)

Figure 9a depicts the liquidus projection of the Al-rich corner of the Al-Ce-Cu phase diagram [36]. The modified diagram proposed by Perrin et al. [35] is also shown in Fig. 9b. According to Fig. 9a and based on the Scheil non-equilibrium solidification approach [35], the solidification of 1Ce and 1.5Ce alloys starts with the formation of α-Al dendritic network. With the progress of the solidification transformation and, accordingly, the enrichment of the interdendritic liquid by Cu and Ce solutes rejected from growing dendrites, the binary eutectic reaction L → α-Al + Al_8CeCu_4 (reaction #2 in Table 6, 16.91 mass % Cu and 7.72 mass % Ce [37]) is preceded by the ternary eutectic reaction L → α-Al + Al_8CeCu_4 + Al_2Cu (reaction #4 in Table 6, 28.42 mass % Cu and 4.57 mass % Ce [37]).

It is worth noting that if the sequence of reactions is followed up by the modified diagram (Fig. 9b), during the binary eutectic reaction #2 (Table 6) Al_8CeCu_3 is formed which then transforms to Al_8CeCu_4 through a peritectoid reaction. More details about this matter will be provided later. Therefore, the α-Al dendritic network, Al_8CeCu_4, and Al_2Cu compounds are the main phases predicted to be formed in the microstructure of 1Ce and 1.5Ce alloys. However, due to the presence of other alloying elements/impurities such as Mn, Fe, and Si in the composition of the experimental alloys, other Ce-containing intermetallics such as AlCeCuSi ($Al_9Ce_2Cu_5Si_3$), $Al_{15}(CuFeMn)_3Si_2$ (reaction #3 in Table 6), and $Al_{24}Cu_8Ce_3Mn$ are also likely to be formed in the microstructure of 1Ce and 1.5Ce samples (Fig. 3c–d and e–f, respectively).

In line with the above, the CA-CCA (Fig. 7b and c) confirms the predicted solidification sequence of 1.0 and 1.5 mass % Ce-added Al 2024 samples. The first peak in Figs. 7b and c appears to be related to the formation of α-Al dendritic networks at about 640 °C. According to the solidification

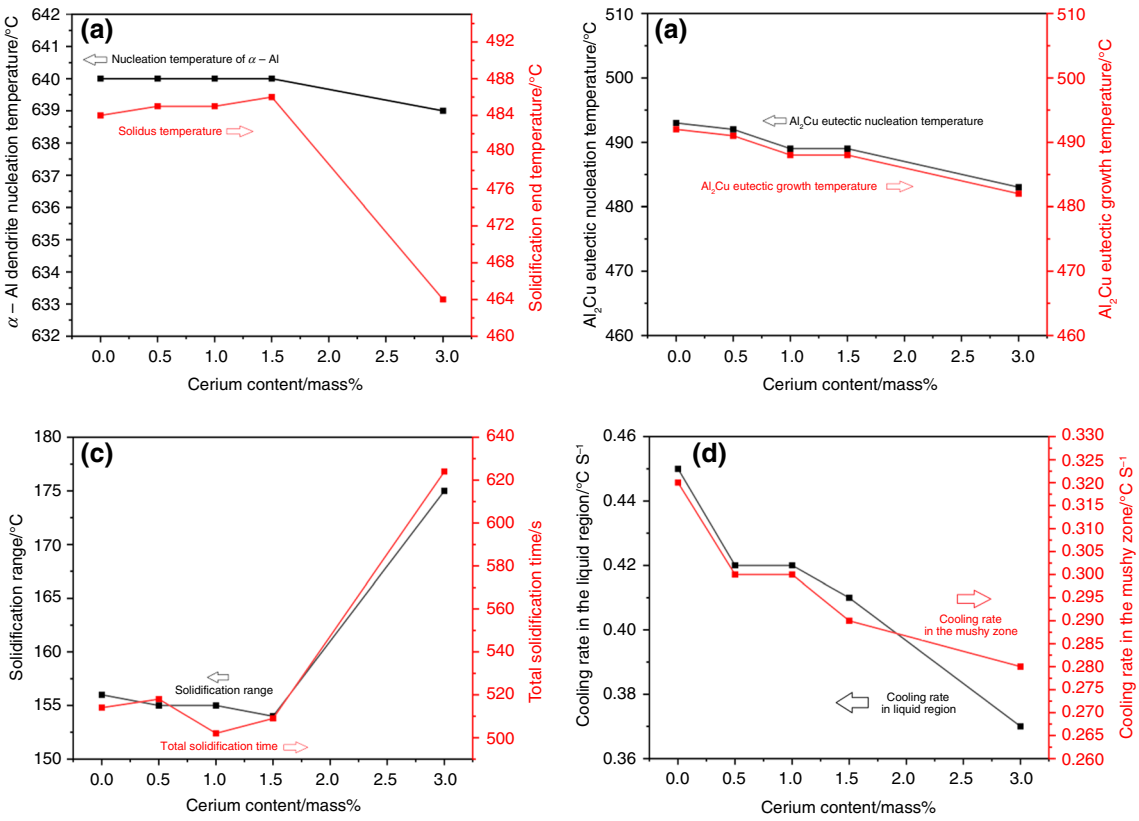

Fig. 10 Effect of Ce content on **a** the nucleation temperature of α-Al and solidus temperature of experimental alloys, **b** the Al_2Cu eutectic nucleation and growth temperatures, **c** the solidification range and total solidification time, and (d) the cooling rate in the liquid and mushy zones

Table 7 Predicted solidification sequences in 3.0Ce samples at the cooling rate of 0.4°Cs^{-1}

Reaction(s) No	Chemical reactions	Reaction temperature (range)/°C
1	$L \rightarrow$ α-Al dendritic networks	639
2	$L \rightarrow$ α-Al + Al_4Ce	604–572
3	$L \rightarrow$ α-Al + $Al_4Ce + Al_8CeCu_4$ (Al_8CeCu_3[a])	
4	$L \rightarrow$ α-Al + Al_8CeCu_4 (Al_8CeCu_3[a])	
5	$L \rightarrow$ α-Al + $Al_{15}(CuFeMn)_3Si_2 + Al_{20}Cu_2Mn_3$ $L + Al_{20}Cu_2Mn_3 \rightarrow$ α-Al + $Al_2Cu + Al_{15}(CuFeMn)_3Si_2$	
6	$L \rightarrow$ α-Al + $Al_8CeCu_4 + Al_2Cu$	535–528
7	$L \rightarrow$ α-Al + Al_2CuMg	514–508
8	$L \rightarrow$ α-Al + $Al_2CuMg + Al_2Cu + Mg_2Si$	483–464

[a]Based on the modified liquidus projection of the Al-rich corner of the Al-Cu-Ce ternary phase diagram (Fig. 9b)

characteristic data obtained from CA-CCA (Fig. 10a), the addition of Ce up to 1.5 mass % did not cause any significant changes in the onset temperature of α-Al dendrites (T_N). The second peak in Fig. 7b and c probably corresponds to the binary eutectic reaction $L \rightarrow$ α-Al + Al_8CeCu_4 (reaction #2 in Table 6) which occurs in the temperature ranges of 582–569 °C and 603–577 °C for the 1Ce and 1.5Ce samples, respectively. After the crystallization of Fe(Mn)-rich $Al_{15}(CuFeMn)_3Si_2$ compound (peak # 3 in Fig. 7b and c), the Al_8CeCu_4 compound is formed as a result of the ternary eutectic reaction $L \rightarrow$ α-Al + $Al_8CeCu_4 + Al_2Cu$ which manifests itself as a peak (peak #4 in the first derivative curve).

The next peaks in the first derivative curves (Fig. 7b and c) can be also attributed to the formation of Al_2CuMg, Al_2Cu, and Mg_2Si compounds through the eutectic reactions e'_3 and E'_1 (Table 6).

The main phases detected in the microstructure of 3.0Ce alloy are marked on micrographs 3g-3h, illustrated in Table 3, and confirmed by the XRD in Fig. 6. Keeping in mind the main detected phases, the liquidus projection of the Al-rich corner of the Al-Cu-Ce ternary phase diagram (Fig. 9a), and concerning the corresponding cooling (first derivative) curves (Fig. 7d), the solidification of 3.0Ce alloy is likely to be started by the development of α-Al dendrites (peak #1 in Fig. 7d) followed by the binary eutectic reaction $L \rightarrow \alpha\text{-Al} + Al_4Ce$ and the ternary eutectic reaction $L \rightarrow \alpha\text{-Al} + Al_4Ce + Al_8CeCu_4$. However, the results of a recent work on the phase stability in Al-rich Al-Cu-Ce alloys [35] show that during the ternary eutectic reaction, Al_8CeCu_3 is formed instead of Al_8CeCu_4 (Fig. 9b). Also, unlike predictions made by the liquidus projection of Al-rich corner of the Al-Cu-Ce ternary phase diagram (Fig. 9a), the sequence of solidification reactions predicted by the modified diagram (Fig. 9b) is in very good agreement with the results of the present research (Fig. 3g–h, Table 3, and Fig. 6).

According to Fig. 9b, following the ternary eutectic reaction #3 in Table 7, the solidification of 3.0Ce alloy progresses with the binary eutectic reaction $L \rightarrow \alpha\text{-Al} + Al_8CeCu_3$ (reaction #4 in Table 7) followed by the formation of the Fe-rich compound $Al_{15}(CuFeMn)_3Si_2$ (reaction #5 in Table 7). Considering the close temperature ranges of reactions #2, #3, #4, and #5 (in Table 7) the second peak (broad peak) in the first derivative curve (Fig. 7d) seemingly belongs to these reactions. It is worth noting that the solidified Al_8CeCu_3 is unstable at lower temperatures and will transform into the stable Al_8CeCu_4 compound through a peritectoid reaction: $Al_8CeCu_3 + Cu$ (dissolved in Al) $\rightarrow Al_8CeCu_4$ (Fig. 9b) [35]. Therefore, the binary eutectic reaction $L \rightarrow \alpha\text{-Al} + Al_8CeCu_3$ is likely to be followed by the peritectoid transformation of Al_8CeCu_3 to Al_8CeCu_4, and the ternary eutectic reaction $L \rightarrow \alpha\text{-Al} + Al_2Cu + Al_8CeCu_4$ (peak #3).

Considering the presence of Mg in the experimental alloy composition (Table 1) and in a similar way to the other Ce-rich alloys, the solidification of 3.0 alloy is likely to be finalized by eutectic reactions #7 and #8 in Table 7 (peaks #4 and #5, respectively). Therefore, in agreement with the microstructural characterization results (Fig. 3g–h, Fig. 6, and Table 3) Ce-rich Al_4Ce and Al_8CeCu_4 intermetallics along with AlCeCuSi and $Al_{24}Cu_8Ce_3Mn$ and Cu-rich compounds Al_2CuMg and Al_2Cu are seen in the microstructure of 3.0Ce alloy.

According to Fig. 10, increasing the Ce content to about 3 mass % significantly affects the solidification characteristic of Al2024 alloy. In spite of a slight decrease in the onset temperature of α-Al dendrites (T_N), it suppresses the nucleation and growth temperatures of the Al_2Cu eutectic (Fig. 10b), prolongs the solidification time by more than 100 s (Fig. 10c), significantly reduces the solidification end temperature (Fig. 10a) and, accordingly, increases the solidification range of the alloy (Fig. 10c). The formation of the Al_4Ce phase is a highly exothermic reaction [40] and is associated with significant latent heat release. Therefore, its formation is likely to slow down the solidification process (Fig. 10d) and provide a higher opportunity for the solute atoms to be rejected from the growing dendrites to the remaining liquid. As a rule of thumb [41], the enrichment of interdendritic liquid pockets at the last stages of the solidification, on the one hand, decreases the nucleation temperature of the Al_2Cu eutectic (Fig. 10b) and, on the other hand, due to increasing the collision/interaction of atoms (crowding effect) negatively affects their free movement/diffusion coefficient [42, 43]. The latter is likely to postpone the growth of Al_2Cu compound.

Considering the negligible solid-solubility of Ce in Al, the rejection and accumulation of Ce atoms (along with other elements) ahead of the solidification front are likely to result significant degree of constitutional undercooling [16]. The combined effect of latent heat release and constitutional undercooling is definitely affected the phases transformation (the geometrical parameters of the precipitates within the as-cast microstructure). More detailed information in this field requires further investigations.

Conclusions

The effect of Ce addition (0.0, 0.5, 1.0, 1.5, and 3.0 mass %) on the microstructure evolution and solidification characteristic of the Al 2024 alloy was investigated using CA-CCA, FE-SEM, EDS, and XRD. The following results can be drawn:

1. Al_2CuMg, Al_2Cu, $Al_{15}(CuFeMn)_3Si_2$, and Mg_2Si are the main intermetallic compounds that are detected in the microstructure of Al 2024 alloy.
2. The addition of Ce up to 1.5 mass % results in the formation of AlCeCuSi ($Al_9Ce_2Cu_5Si_3$), Al_8CeCu_4, and $Al_{24}Cu_8Ce_3Mn$ Ce-rich compounds in the microstructure of Al 2024 alloy. Further addition of Ce up to 3.0 mass % promotes the formation of another Ce-rich compound Al_4Ce in the microstructure.
3. The correlation between the Ce concentration and solidification parameters of intermetallics in Al 2024 alloy is derived to predict solidification behavior in the presence of Ce.

4. The temperature range and sequence of reactions during which various intermetallic compounds, especially Ce-rich compounds, are formed, were determined.

References

1. Zamani M, Toschi S, Morri A, Ceschini L, Seifeddine S. Optimisation of heat treatment of Al–Cu–(Mg–Ag) cast alloys. J Therm Anal Calorim. 2020;139:3427–40.
2. Ghosh KS. Calorimetric studies of 2024 Al–Cu–Mg and 2014 Al–Cu–Mg–Si alloys of various tempers. J Therm Anal Calorim. 2019;136:447–59.
3. Shabestari SG, Ghoncheh MH, Momeni H. Evaluation of formation of intermetallic compounds in Al2024 alloy using thermal analysis technique. Thermochim Acta. 2014;10(589):174–82.
4. Czerwinski F. Cerium in aluminum alloys. J Mater Sci. 2020;55(1):24–72.
5. Fang MM, Yan H, Song XC, Sun YH. Effect of (Pr+ Ce) additions on microstructure and mechanical properties of AlSi5Cu1Mg alloy. App Sci. 2019;9(9):1856.
6. Hu B, Zhu WJ, Li ZX, Lee SB, Li DJ, Zeng XQ, Choi YS. Effects of Ce content on the modification of Mg2Si phase in Mg-5Al-2Si alloy. J Mag Alloys. 2021;7:2299.
7. Alkahtani SA, Elgallad EM, Tash MM, Samuel AM, Samuel FH. Effect of rare earth metals on the microstructure of Al-Si based alloys. Mater. 2016;9(1):45.
8. Wang WT, Zhang XM, Gao ZG, Jia YZ, Ye LY, Zheng DW, Liu L. Influences of Ce addition on the microstructures and mechanical properties of 2519A aluminum alloy plate. J Alloys Comp. 2010;491(1–2):366–715.
9. Xiao D, Wang J, Ding D, Yang H. Effect of rare earth Ce addition on the microstructure and mechanical properties of an Al–Cu–Mg–Ag alloy. J Alloys Compd. 2003;352:84–8.
10. Xiao D, Wang J, Ding D. Effect of minor cerium additions on microstructure and mechanical properties of cast Al–Cu–Mg–Ag alloy. Mater Sci Technol. 2004;20(10):1237–40.
11. Yu X, Dai H, Li Z, Sun J, Zhao J, Li C, Liu W. Improved recrystallization resistance of Al–Cu–Li–Zr alloy through Ce addition. Metals. 2018;8(12):1035.
12. Wang W, Zhang X, Gao Z, Jia Y, Ye L, Zheng D, Liu L. Influences of Ce addition on the microstructures and mechanical properties of 2519A aluminum alloy plate. J Alloys Compd. 2010;491(1–2):366–71.
13. Vončina M, Medved J, Steinacher M, Ozimič K. The influence of La and Ce additions on the solidification of alloys from the Al–Fe system. J Therm Anal Calorim. 2024;26:1.
14. Belov NA, Aksenov AA, Eskin DG. Iron in aluminium alloys: impurity and alloying element. London: CRC Press; 2002.
15. Goto S, Kim B, Park H, Belov NA, Zolotorevkij VS, Aso S, Komatsu Y. Application of eutectics to development of high strength cast aluminum alloys. J Soci Mater Eng Res Japan. 2002;15(2):66–73.
16. Niu G, Mao J, Wang J. Effect of Ce addition on fluidity of casting aluminum alloy A356. Metall Mater Trans A. 2019;50:5935–44.
17. Zeng Z, Pan H, Pan Z, Wang S, Huang Y, Tang W, Yang C, Ren Y, Qin G. Effect of Sm and Ce content on microstructure and mechanical property of newly developed Mg-Sm-Ce-Mn based alloy. Mater Character. 2023;1(206): 113420.
18. Wang C, Zeng L, Zhang W, Tang F, Ding W, Xiao S, Liang T. Enhanced mechanical properties and corrosion resistance of rolled Mg-1.5 Sn-0.5 Ca alloy by Ce microalloying. Mater Character. 2021;179:111325.
19. Del Olmo R, Mohedano M, Visser P, Rodriguez A, Matykina E, Arrabal R. Effect of cerium (IV) on thin sulfuric acid anodizing of 2024–T3 alloy. J Mater Res Technol. 2021;15:3240–54.
20. Wang K, Wei M, Liao Z, Jin S, Wan B, Lei Z, Tang P, Tian J, Zhang L, Li W. A comparative study of iron, cobalt or cerium micro-alloying on microstructure and apparent viscosity of Al-5Ni alloy. J Alloys Comp. 2023;952: 170052.
21. Luo S, Wang L, Cao Y. Effect of Zr grain refinement on solidification behavior of Mg–3Nd alloy by cooling curve thermal analysis. J Therm Anal Calorim. 2023;148(10):4049–58.
22. Mostafapoor S, Malekan M, Emamy M. Effects of Zr addition on solidification characteristics of Al–Zn–Mg–Cu alloy using thermal analysis. J Therm Anal Calorim. 2018;134:1457–69.
23. Li J, Chen R, Ma Y, Ke W. Computer-aided cooling curve thermal analysis and microstructural characterization of Mg–Gd–Y–Zr system alloys. Thermochim Acta. 2014;20(590):232–41.
24. Farahany S, Ghandvar H. On the effect of praseodymium on solidification characteristics, microstructure, and mechanical properties of commercial ADC12 alloy. J Therm Anal Calorim. 2023;148(12):5247–55.
25. Elesbão DS, Kakitani R, Cheung N, Garcia A, de Barcellos VK, da Costa EM, dos Santos CA. Influence of Cu and Cr contents on the solidification path and microstructure formation of hypoeutectic as-cast Al–Cu–Cr alloys. J Therm Anal Calorim. 2023;148(18):9403–21.
26. Mahmoud MG, Mosleh AO, Pozdniakov AV, Khalifa W, Mohamed MS. Characterization of the solidification behavior, microstructure and mechanical properties of aluminum alloy 6063 with samarium addition. J Alloys Comp. 2022;25(929): 167234.
27. Ghoncheh MH, Shabestari SG, Abbasi MH. Effect of cooling rate on the microstructure and solidification characteristics of Al2024 alloy using computer-aided thermal analysis technique. J Therm Anal Calorim. 2014;117:1253–61.
28. Ghoncheh MH, Shabestari SG. Effect of cooling rate on the dendrite coherency point during solidification of Al2024 alloy. Metal Mater Trans A. 2015;46:1287–99.
29. Amin KM, Mufti NA. Investigating cooling curve profile and microstructure of a squeeze cast Al–4% Cu alloy. J Mater Proc Technol. 2012;212(8):1631–9.
30. Meetsma A, De Boer JL, Van Smaalen S. Refinement of the crystal structure of tetragonal Al2Cu. J Solid State Chem. 1989;83(2):370–2.
31. Hu Y, Wu S, Shen Z, Cao H, Zhong X, Withers PJ. Fine equiaxed zone induced softening and failure behavior of 7050 aluminum alloy hybrid laser welds. Mater Sci Eng A. 2021;21(821): 141597.
32. Morris RG, Redin RD, Danielson GC. Semiconducting properties of Mg 2 Si single crystals. Phys Rev. 1958;109(6):1909.
33. Mrówka-Nowotnik G, Sieniawski J. Analysis of intermetallic phases in 2024 aluminium alloy. Solid State Phenom. 2013;11(197):238–43.
34. Henderson HB, Hammons JA, Baker AA, McCall SK, Li TT, Perron A, Sims ZC, Ott RT, Meng F, Thompson MJ, Weiss D. Enhanced thermal coarsening resistance in a nanostructured aluminum-cerium alloy produced by additive manufacturing. Mater Des. 2021;1(209): 109988.
35. Perrin A, Bahl S, Leonard DN, Michi R, Sisco K, Plotkowski A, Shyam A, Dehoff R, Shin D, Yang Y. Phase stability in cast and additively manufactured Al-rich Al-Cu-Ce alloys. J Alloys Comp. 2022;10(926): 166984.
36. Belov NA, Khvan AV. The ternary Al–Ce–Cu phase diagram in the aluminum-rich corner. Acta Mater. 2007;55(16):5473–82.
37. Zolotorevsky VS, Belov NA, Glazoff MV. Casting aluminum alloys. Amsterdam: Elsevier; 2007.
38. Sims ZC, Weiss D, McCall SK, McGuire MA, Ott RT, Geer T, Rios O, Turchi PA. Cerium-based, intermetallic-strengthened

aluminum casting alloy: high-volume co-product development. JOM. 2016;68:1940–7.
39. Belov NA, Eskin DG, Aksenov AA. Multicomponent phase diagrams: applications for commercial aluminum alloys. 1st ed. Boston: Elsevier; 2005. p. 167.
40. Liang Y, Shi Z, Li G, Zhang R, Li M. Effects of rare earth modification on microstructure refinement and mechanical properties of Al-2 wt% Fe alloys. Mater Res Exp. 2019;6(10): 106504.
41. Nafisi S, Ghomashchi R. Semi-solid processing of aluminum alloys. Swizerland: Springer International Publishing; 2016. p. 104.
42. Schiller T, Sondermann E, Meyer A. New analyzing approaches for in situ interdiffusion experiments to determine concentration-dependent diffusion coefficients in liquid Al–Au. Metals. 2021;11(11):1772.
43. Stelian C, Duffar T. Numerical analysis of solute distribution and interface stabilization during experimental Bridgman growth of concentrated GaInSb alloys. J Cryst Growth. 2005;275(1–2):e585–94.